

# Tilt series STEM simulation of a $25 \times 25 \times 25$ nm semiconductor with characteristic X-ray emission



R. Aveyard, B. Rieger\*

Department of Imaging Physics, Delft University of Technology, 2628CJ Delft, The Netherlands

## ARTICLE INFO

### Article history:

Received 19 April 2016

Received in revised form

5 September 2016

Accepted 11 September 2016

Available online 13 September 2016

### Keywords:

HAADF

STEM

Simulation

X-ray

EDS

Semiconductor

Tomography

## ABSTRACT

The detection and quantification of fabrication defects is vital to the ongoing miniaturization of integrated circuits. The atomic resolution of HAADF-STEM combined with the chemical sensitivity of EDS could provide the means by which this is achieved for the next generation of semiconductor devices. To realize this, however, a streamlined acquisition and analysis procedure must first be developed. Here, we report the simulation of a HAADF-STEM and EDS tilt-series dataset of a PMOS finFET device which will be used as a testbed for such a development. The methods used to calculate the data and the details of the specimen model are fully described here. The dataset consists of 179 projections in  $2^\circ$  increments with HAADF images and characteristic X-ray maps for each projection. This unusually large calculation has been made possible through the use of a national supercomputer and will be made available for the development and assessment of reconstruction and analysis procedures for this highly significant industrial application.

© 2016 Elsevier B.V. All rights reserved.

## 1. Introduction

The continuing miniaturization of integrated circuits places ever greater demands on manufacturing techniques. An important aspect of successful manufacturing processes is a method with which defects can be detected and characterized. The defects in current and next-generation integrated circuits can be both geometrical and chemical, and have dimensions of the order of a few nanometers. To resolve such small defects, new characterization procedures are needed. High-angle annular dark field (HAADF) scanning transmission electron microscopy (STEM) offers atomic resolution images which are projections through the specimen. The three-dimensional information imparted in these projections can be used in a rotational tomography framework to yield three-dimensional reconstructed objects. X-ray spectra can be recorded concurrently with HAADF images and provides the highly sensitive chemical composition information which is crucial to defect detection. Recent developments in X-ray detector technology have reduced acquisition times making tomographic energy dispersive spectroscopy (EDS) feasible [1]. The synergistic fusion of the two data types could provide extra information for the reconstruction process [2].

The accuracy of the reconstruction process is fundamentally limited by the quality of the tilt-series dataset. Tomographic

reconstruction implicitly assumes that each pixel in the tilt-series images represents a linear projection of the specimen. In practice, reconstructions can be performed with some success so long as the imaging signal varies monotonically with mass-thickness in the sample. To meet this requirement in STEM, a HAADF detector should be used to minimize coherent contributions to the imaging signal, and so reliably yield monotonic projections [3]. The HAADF signal is still susceptible to non-linearities, particularly for specimens with a crystalline zone-axis aligned with the optical axis, which causes channelling effects [4,5]. At large specimen thicknesses signal non-linearity can also occur due to multiple scattering events redirecting electrons outside the range of the annular detector, leading to a damped signal at greater thicknesses and cupping artefacts in reconstructed volumes [6]. In addition to signal non-linearity, the accuracy of reconstructions can be adversely affected by the limited angular range of experimental tilt-series which causes missing wedge artefacts in the reconstruction.

Atom probe tomography offers a means by which the accuracy of reconstructions in HAADF-STEM tomography can be established. However, the specimen preparation required for this technique complicates such an approach. Moreover, complex samples cannot be fabricated to known specifications with sufficiently tight tolerances to provide standards. Computational simulations offer a more accessible solution. Here we report the simulation of tomographic tilt-series for a large ( $25 \times 25 \times 25$  nm) and well defined semiconductor specimen.

The simulation of image formation in STEM is well established, and has proven successful in reproducing experimentally observed

\* Corresponding author.

E-mail address: [b.rieger@tudelft.nl](mailto:b.rieger@tudelft.nl) (B. Rieger).

features in absolute terms [7]. The ionization of atoms in a specimen by incident electron beams, the excitation which leads to characteristic X-ray emission, has been included in Bloch wave calculations by Malsen and Rosouw, Manson, and Saldin and Rez [8–10]. More recently, atomic ionization has been incorporated into multislice calculations by Allen et al. through the use of ionization scattering factors [11]. An alternative approach including ionization in the multislice framework using projected matrix elements has been developed by Dwyer and used to simulate electron energy loss spectroscopy [12]. Multislice calculations of EDS have recently been produced using the multislice ionization procedure developed by Allen et al., and were found to give a good agreement with experimental data on an absolute scale [13]. The program used in this work adopts a similar approach, however, rather than using the quantum excitation of phonons model, the numerically equivalent frozen phonon algorithm is used to account for the thermal motion of atoms in the specimen.

The computational expense of performing a tomographic series of multislice simulations including atomic ionizations for relatively large specimens ( $25 \text{ nm}^3$ ) is considerable. Consequently, the large tomographic dataset which is described here is made available to the scientific community upon request, for the development and assessment of reconstruction and analysis techniques. This report will begin by detailing the construction of the semiconductor specimen model before introducing the simulation methods, the calculation parameters chosen for the simulation, and practical computational considerations. Finally, the resulting dataset will be discussed.

## 2. Model construction

The specimen model consists of a  $\sim 25 \times 25 \times 25 \text{ nm}$  region of a PMOS finFET, as shown in Fig. 1. The crystalline silicon region (yellow spheres) constitutes the source-drain fin. This is coated in a thin oxide layer (red), on top of which is a 2 nm layer of high dielectric constant amorphous hafnium (white) dioxide. This is coated in a metal gate consisting of a 2 nm layer of amorphous tantalum (pink). The remaining volume is filled with polycrystalline titanium (bronze) aluminium (grey) nitride (blue),  $\text{TiAlN}_2$ .

The structure was generated starting with the silicon fin, which was cut directly from a bulk crystal with arbitrary roughening applied. Subsequent layers were added by generating larger-than-necessary regions of each material, removing any atoms overlapping those in the preceding layer, and removing any atoms with a separation greater than the desired layer thickness from any atom in the preceding layer. No structural relaxations were applied so the interfaces are physically unrealistic, however, this is of no consequence to either image formation or reconstruction.

To produce the amorphous regions, the total volume was divided into a grid of voxels with dimensions equal to  $2/3$  of the smallest nearest neighbour distance of the material. Random Cartesian coordinates were then generated in any empty voxel. The coordinates were discarded if they were closer than the nearest neighbour distance to atoms already present in the neighbouring two layers of voxels. After 100 failed attempts to generate coordinates in an empty voxel, it is excluded from further attempts. This algorithm avoids the diminishing returns associated with an unrestricted random generation of coordinates, allowing the models to achieve full densities in a reasonable time frame. Elements were assigned to achieve the desired chemical ratios, however, bond angles and local densities of each species were not controlled, only nearest neighbour distances. Whilst this does not result in a chemically realistic structure, it is sufficiently accurate for image simulation and analysis purposes.

To generate the polycrystalline region, random coordinates were generated within the desired volume, with a separation no smaller than 5 nm. These points were used as the seeds around which Voronoi cells were generated. A bulk crystalline model was translated to the position of each Voronoi cell, and rotated by a random magnitude about a random axis. The bulk crystal was then cut to the dimensions of the Voronoi cell. This results in an approximately isotropic polycrystalline material with no relationship between the orientations of neighbouring crystallites, and no interfacial distortions.

A number of defects have been introduced into the model. There are 3 pinhole defects in the high dielectric  $\text{HfO}_2$  insulating layer with diameters of 1 nm, 2 nm, and 3 nm. These holes are filled with tantalum, as would occur during tantalum deposition. A region of the  $\text{HfO}_2$  layer has also been thinned to a single atomic thickness. The final defect is a carbon nanoparticle contaminant trapped between the  $\text{HfO}_2$  and Ta layers. The nanoparticle is an amorphous ellipsoid with a diameter of  $\sim 7 \text{ nm}$ . All the defects are offset along the tilt axis so that they remain independent in all projections.

## 3. Multislice simulations

Due to the non-periodic nature of the semiconductor specimen, the program used to perform the calculations reported here has been developed using the multislice protocol. At each incident scanning position,  $\mathbf{x}_p$ , an electron wavefunction is generated in reciprocal space as the sum of plane waves with phase offsets to account for focussing and aberrations:

$$\psi(\mathbf{x}, \mathbf{x}_p) = A_p \int_0^\alpha \exp(i2\pi\mathbf{k} \cdot (\mathbf{x} - \mathbf{x}_p) - i\chi(\mathbf{k})d^2\mathbf{k}). \quad (1)$$

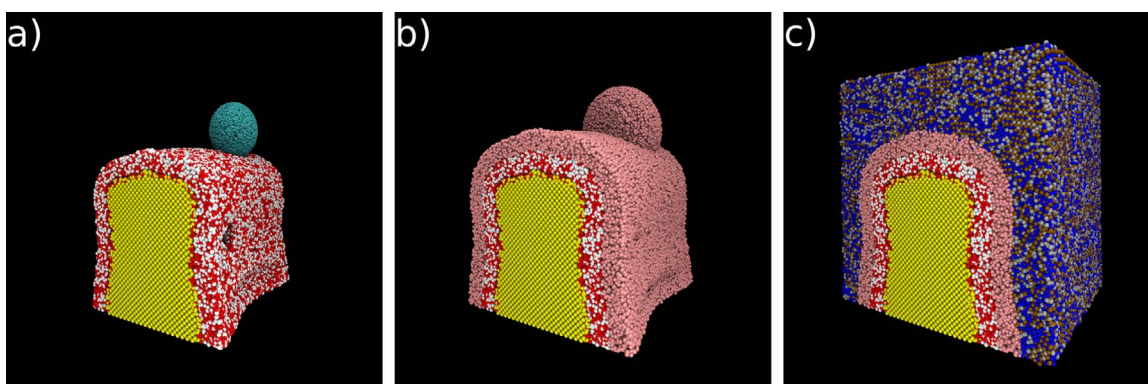


**Fig. 1.** Atomic model of finFET structure (a)  $\text{HfO}_2$  layer with pinholes and carbon nanoparticle contaminant, (b) Ta layer fills pinholes in  $\text{HfO}_2$  layer, (c) Remaining volume filled with polycrystalline  $\text{TiAlN}_2$ .

Where  $A_p$  is a normalization constant,  $\alpha$  is the focussed beam convergence angle, and  $\chi$  is the aberration function accounting for phase offsets due to defocus, astigmatism, and other aberrations. The specimen is described by a series of thin potential slices,  $t_z(\mathbf{x})$ , transverse to the optical axis. Each slice consists of a superposition of the projected scattering potentials,  $v_{zj}$ , of the atoms that are closer to that slice than any other:

$$t_z(\mathbf{x}) = \exp(i\sigma v_z(\mathbf{x})) \quad (2)$$

$$v_z(\mathbf{x}) = \sum_{j=1}^N v_{zj}(\mathbf{x} - \mathbf{x}_j). \quad (3)$$

Where  $\mathbf{x}_j$  is the position of atom  $j$  transverse to the optical axis, and  $\sigma$  is the interaction parameter. The projected potentials are calculated via integration and Fourier transform of the scattering factors collated by Kirkland [14]. In accordance with the weak phase object approximation, the interaction of the electron beam with a slice of the specimen results in a phase shift of the beam and is calculated by the convolution of the electron wavefunction with the scattering potential slice [15]. This is computed by a point-wise multiplication of the Fourier transform:

$$\psi_t(\mathbf{k}, \mathbf{x}_p) = \int_0^{x_{\max}} d^2\mathbf{x} \int_0^{k_{\max}} \exp(-2\pi i\mathbf{x}\cdot\mathbf{k}) \psi(\mathbf{k}, \mathbf{x}_p) d^2\mathbf{k} \cdot t_z(\mathbf{x}). \quad (4)$$

After interaction with the scattering potential slice, the wavefunction is propagated the small distance to the next slice via a point-wise multiplication with a Fresnel-Kirchhoff propagation array,  $P(\mathbf{k}, \Delta z)$ , in reciprocal space [14]:

$$\psi_{z+\Delta z}(\mathbf{k}, \mathbf{x}_p) = \psi_t(\mathbf{k}) \cdot P(\mathbf{k}, \Delta z). \quad (5)$$

After iteratively interacting and propagating through the entire specimen, the intensity of the wavefunction in reciprocal space is equivalent to the angular distribution of the electron beam arriving at the detector plane. The intensity of the electron beam impinging on the detector is the squared modulus of the wavefunction within the angular range of the annular detector.

Simulating the production of characteristic X-rays requires determining the probability that atoms inside the specimen are ionized by the electron beam, and then accounting for the probability of characteristic X-ray emission, given the ionization probability.

The probability that ionization occurs is determined using tabulated ionization scattering factors [16,17]. For every scattering potential slice in the multislice algorithm, a series of projected ionization potential slices are constructed, one for each element present in the sample. The probability of ionization of a given element,  $m$ , is calculated via a point-wise multiplication of the ionization potential slice with the electron beam intensity. This is calculated immediately before the beam is scattered in Eq. (4)

$$P_m(\mathbf{x}_p) = \int_0^{x_{\max}} d^2\mathbf{x} \left| \int_0^{k_{\max}} \exp(-2\pi i\mathbf{x}\cdot\mathbf{k}) \psi(\mathbf{k}, \mathbf{x}_p) d^2\mathbf{k} \right|^2 \cdot I_{z,m}(\mathbf{x}). \quad (6)$$

Here,  $I_{z,m}(\mathbf{x})$  is the projected ionization potential at slice  $z$  for element  $m$ . Note that the ionization interaction does not alter the electron wavefunction in this model. To calculate the yield of characteristic X-ray emission the ionization probability is modulated by characteristic X-ray fluorescence yields

$$X_{m,c}(\mathbf{x}_p) = P_m(\mathbf{x}_p) \cdot Y_c. \quad (7)$$

Where  $X_{m,c}$  is the yield of characteristic X-ray emissions for atom  $Z$  with fluorescence yield  $Y_c$ . The variable 'c' denotes the characteristic X-ray line. The tilt-series datasets reported here use fluorescence yields for K- and L- shell emission compiled by Elam et al. [18]. The probability of emission from individual orbitals can

also be calculated using the appropriate fluorescence yield values.

Naive EDS maps are generated by summing the probability of characteristic emission from each slice, at each incident electron position. For more accurate results the effects of X-ray absorption in the sample, the limited angular range of the detector, and the detector efficiency must be accounted for [19]. This can be achieved by recording the X-ray emission yield,  $X_{m,c}$ , at each slice, allowing for simulation of these effects, however, this entails substantially greater computational expense which is not feasible during the already large calculations described here.

Thermal vibrations of the atoms in the specimen are accounted for using the frozen phonon algorithm in which a number of simulations with small random perturbations of the atomic coordinates are performed, and the results of each configuration are incoherently averaged, to give the final projection.

#### 4. Simulation details

The tilt-series dataset described here consists of 179 projections in  $2^\circ$  increments to give a full  $360^\circ$  range. Each projection consists of a simulated HAADF-STEM image and 11 characteristic X-ray yield maps. The simulations were performed with an accelerating voltage of 200 keV, this was selected to match the settings used in previously reported experimental acquisitions of HAADF-STEM with EDS for finFET devices [20]. A low convergence angle of 10 mrad was selected as it represents a good compromise between depth of field and transverse resolution. No beam aberrations were included. In each projection the beam is focussed on the uppermost point of the specimen and the focal plane is uniform for the entire projection. The electron wavefunction was normalised to a total intensity of 1, thus the recorded signal directly gives the fraction of the incident intensity that reaches the detector. A HAADF detector geometry was chosen with an inner angle of 90 mrad to minimize coherent contributions and a resolution-limited outer angle of 230 mrad.

The scattering potential of the specimen was limited by a frequency cut-off at 230 mrad and sampled with 3.6 pm/pixel. The focussed electron probe was sampled by a  $256 \times 256$  pixel array over  $9.3 \times 9.3 \text{ \AA}$  in real space. The limited extent of the real space sampling resulted in a loss of intensity of no more than 2% in any projection. Thermal vibrations of the specimen were accounted for using 10 frozen phonon configurations with bulk Debye-Waller factors at 295 K taken from the literature [21–25].

#### 5. Computational considerations

For each of the 179 projections in the tilt series, 10 frozen phonon configurations are required. Each configuration involves the propagation of a focussed electron beam from  $512 \times 512$  scanning positions. At each position the wavefunction interacts with between 78 and 126 slices, requiring two Fourier transforms and two point-wise multiplications per slice. A further point-wise multiplication is required for each of the 8 ionization potential slices. In total, the tilt series involves the calculation of  $\sim 1 \times 10^{11}$  Fourier transforms of a  $256 \times 256$  array, and  $\sim 5 \times 10^{11}$  point-wise multiplications of the same size.

The propagation-interaction through the specimen must be performed sequentially, but the scan over different incident positions can be calculated simultaneously. This was implemented on the Dutch national supercomputer, Cartesius. Each projection was assigned to a node with 32 Intel Xeon E5-4650 CPU cores and a memory of 256 GB. The independent beam propagations were split between the 32 cores using the openMP application

programming interface. In total, the tilt-series used  $\sim 90,000$  core hours, equivalent to 10 years of serial computation. The number of nodes used concurrently varied with availability at the super-computer facility. The whole calculation was completed in 6 days, commensurate with the use of  $\sim 20$  nodes, averaged over the period.

## 6. Results

Fig. 2 shows example HAADF projections of the finFET device for an annular detector range of  $90\text{--}230$  mrad.

The  $0^\circ$  projection has the silicon source-drain fin aligned along the optical axis. The contrast in HAADF-STEM is caused by Coulomb scattering of the electron beam by nuclei in the sample, consequently, it is approximately proportional to the square of the atomic number,  $Z$ . The layers of tantalum ( $Z=73$ ) and hafnium

( $Z=72$ ) dioxide are clearly visible as bright arches in the image. The outline of the carbon nanoparticle is also clearly defined due to the tantalum coating. In comparison, the  $\text{TiAlN}_2$  polycrystalline ( $Z=22,13,7$ ), the carbon particle itself ( $Z=6$ ), and the silicon fin ( $Z=14$ ) produce little contrast. Exceptions occur in the cases where the crystalline silicon is aligned with a zone-axis parallel to the optical axis, such as in the  $0^\circ$  projection, where channelling effects substantially enhance contrast and bright spots corresponding to atomic columns can be seen.

Fig. 3 shows the EDS maps acquired simultaneously to the  $0^\circ$  HAADF image in Fig. 2. The K- and L- lines for Ti, Hf, and Ta have been combined. The superposition of all the EDS maps, shown in the centre of Fig. 3 highlights the potential value of this chemically sensitive modality for inspecting complex semiconductor devices.

The channelling effect highlights the inherent non-linearity in the HAADF signal, which is present, though not necessarily significant, in all regions of the specimen, in all of the projections.

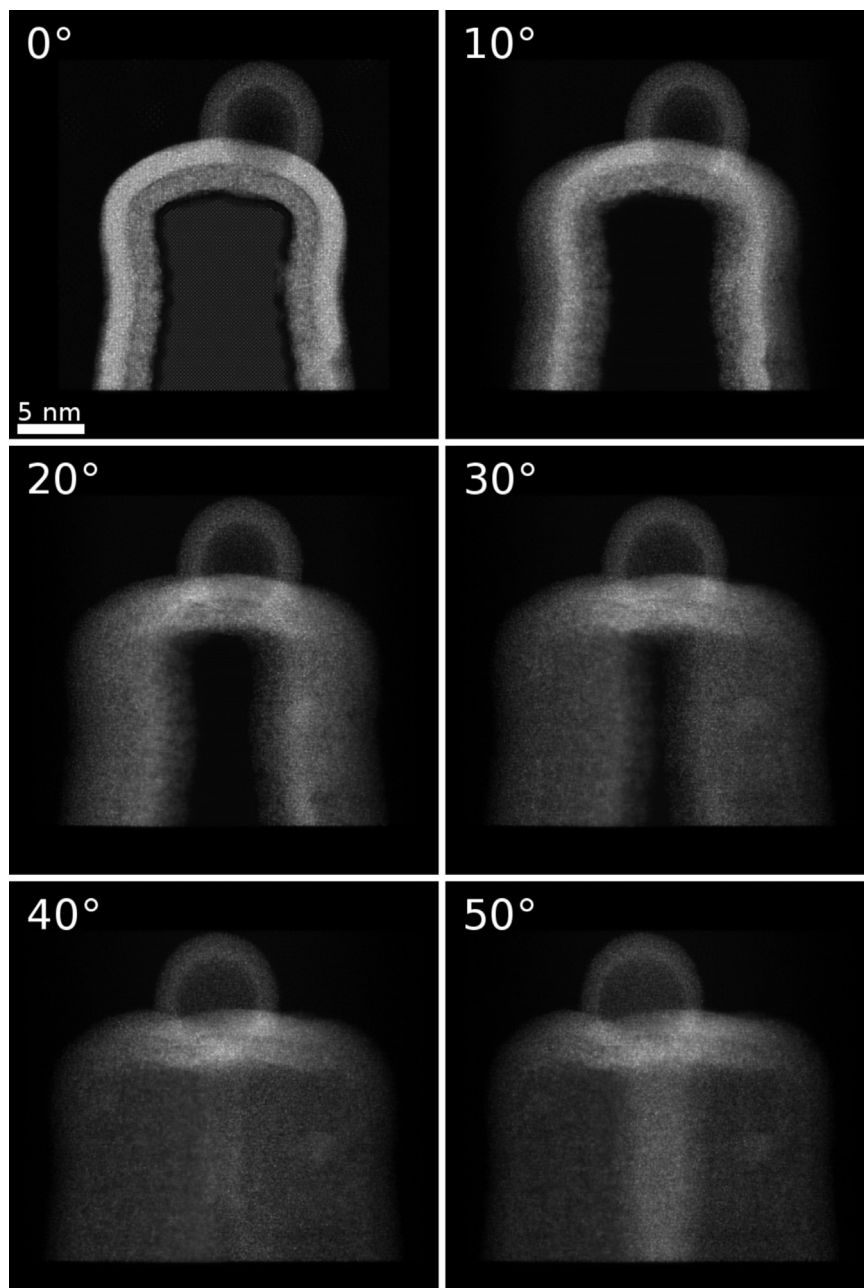
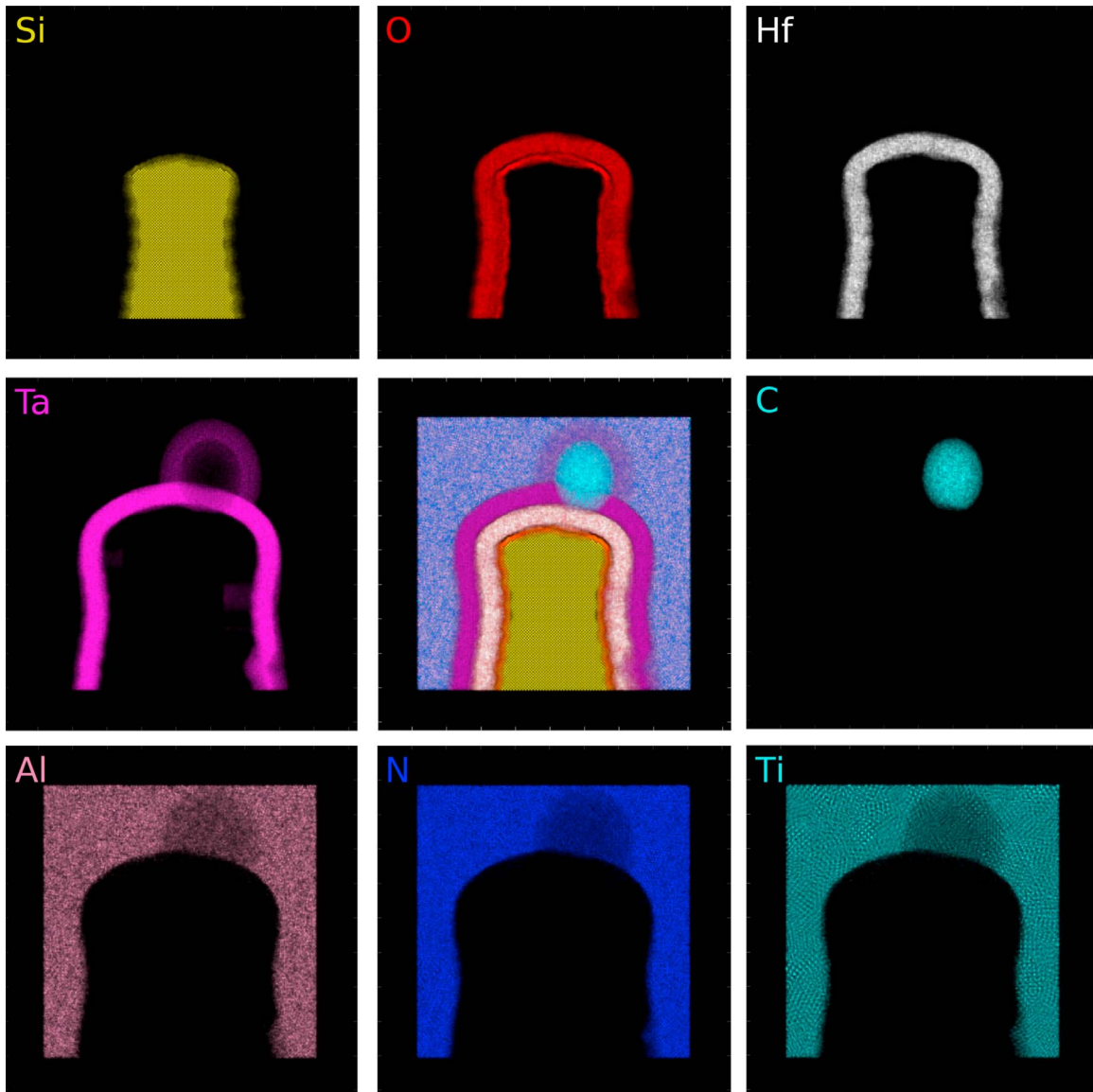
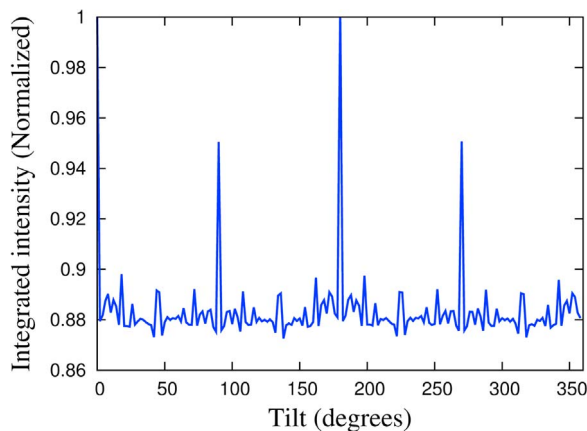


Fig. 2. HAADF-STEM projections of the finFET model.



**Fig. 3.** EDS maps for the 0° projection. K- and L- lines have been combined where both are present. The central image is a qualitative superposition of all the EDS maps.



**Fig. 4.** The image-integrated intensities of the HAADF tilt series exhibit substantial signal enhancement at zone-axis orientations.

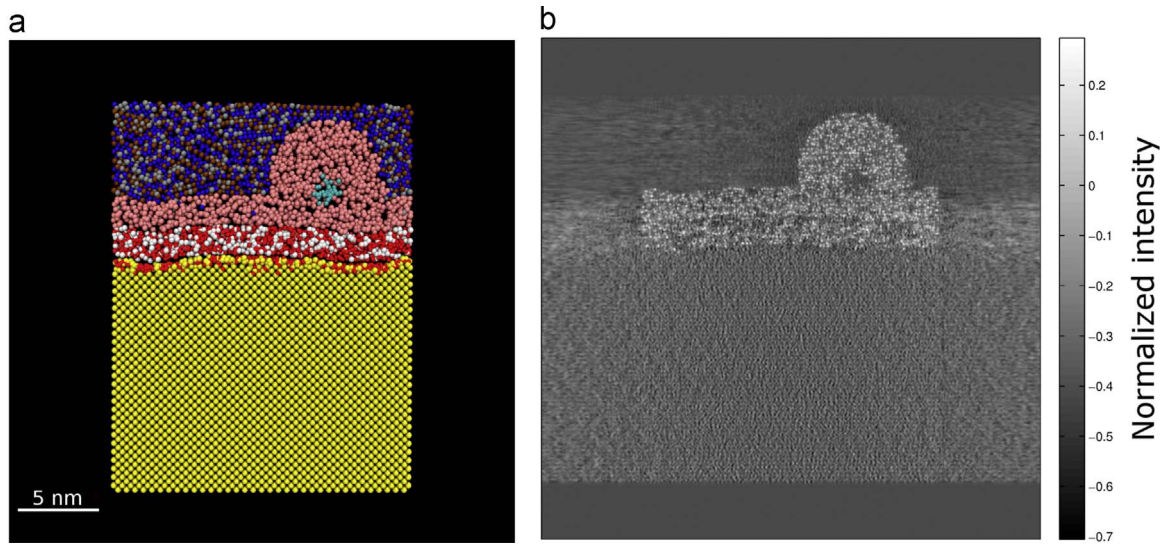
discerned by observing the variation of the image-integrated intensities, as shown in Fig. 4.

As the total mass-thickness of the object is the same for all the projections, the image-integrated intensity should ideally be tilt-invariant. The non-linear effects observed here cannot be corrected by a simple scaling of image intensities because the contrast enhancement is not uniformly distributed through the image, crystalline regions are strongly affected whilst amorphous regions exhibit more linear behaviour. Consequently, it can be advantageous to exclude zone-axis projections when performing tomographic reconstructions [26,27].

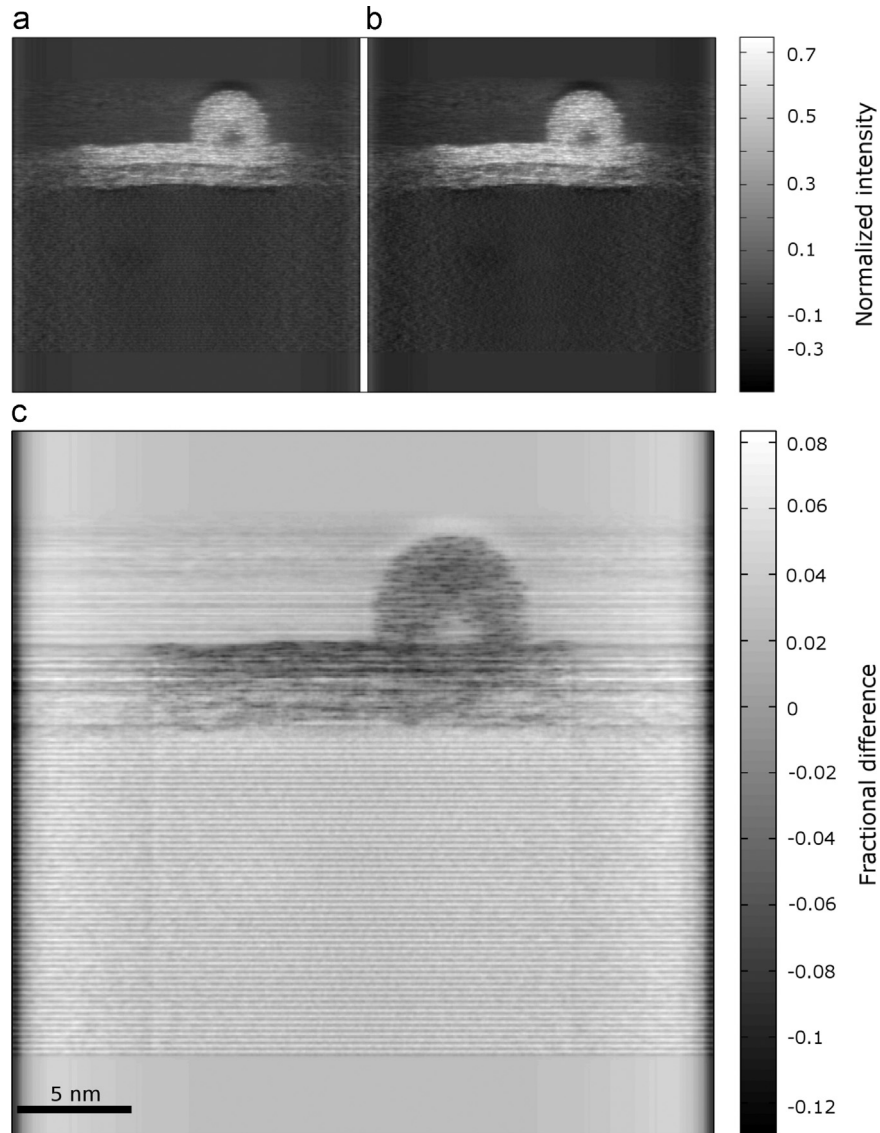
To demonstrate the results of conventional tomographic reconstructions, both weighted back projection (WBP) and simultaneous iterative reconstruction technique (SIRT) algorithms have been applied to the simulated dataset. The reconstructions were performed using the algorithms implemented in the Inspec3D V4.1 software produced by FEI, which in turn are based on the ASTRA toolbox [28,29]. The SIRT reconstruction was performed using 50 iterations, which we found to give the best tradeoff between contrast and resolution.

Fig. 5a shows a  $\sim 2.5$  Å thick slice through the centre of the atomistic model, Fig. 5b shows the corresponding slice from the

This is unavoidable as the probing beam is necessarily modified by the scattering events which yield the signal. The challenges this presents to accurate reconstruction of the object are clearly



**Fig. 5.** Comparison of a slice of the atomistic model, (a), with the corresponding slice of a WBP reconstruction, (b). The poor contrast in regions of lighter elements demonstrates the difficulty in segmenting the component layers of the device.



**Fig. 6.** (a) A typical slice through the centre of a SIRT reconstruction exhibits streaking when zone-axis images are included. (b) With zone-axis projections removed, the channelling artefacts are avoided. (c) The magnitude of the streaking artefacts caused here by channelling are on the order of 2%.

WBP reconstruction of the full 360° tilt-series with projections in 2° increments using a full ramp filter.

It can be seen that the outer shape of the tantalum and hafnium slices are recovered, though the HAADF signal alone does not allow for the two elements to be distinguished. The large contrast generated by these heavy element regions introduces artefacts throughout the volume which obscure the geometry of the lighter regions. This makes segmentation of the component layers difficult without reference to EDS data.

Fig. 6a shows a slice through the centre of the SIRT reconstruction of the full 360° tilt-series with projections in 2° increments. Fig. 6b shows the same slice generated from the same tilt-series, but with the 4 projections exhibiting strong channelling enhancements excluded from the reconstruction.

Upon close inspection it can be seen that the channelling induced intensity enhancement in the zone-axis images results in streaked stripes of bright contrast through the silicon region of the reconstructed object. The stripes are more readily discerned in the difference image shown in Fig. 6c. The streaks extend beyond the boundaries of the object, through the entire reconstruction volume. It can be seen from Fig. 6 that the ~10% enhancement in intensities in the zone-axis images causes streaks of ~2% in the reconstruction of the 179-projection series. It should be noted that, as a relatively light element, crystalline silicon is less susceptible to channelling than crystals of heavier elements, for which the channelling artefacts in reconstructions are likely to be more pronounced, particularly for reconstructions from fewer projections.

## 7. Discussion

The simulated data reported here has a number of unrealistic characteristics that do not reflect typical experimental data and some post-processing should be applied in order to produce results more comparable to an experimental acquisition. The data is provided in its raw form so that a variety of effects can be implemented to meet different requirements.

The as-provided dataset does not include the smearing caused by the energy spread and finite dimensions of real electron sources. This can be applied by convolving the projections with an effective source function, which can be empirically derived [30]. Similarly, arbitrary levels of shot noise can be introduced to the raw dataset using a Poisson distribution to reflect the desired electron dose [26].

The EDX dataset consists of maps of projected characteristic X-ray emission. The absorption of X-rays in the sample, the limited angular range of the detector, and the detector efficiency are not included and would degrade the measured signal. These effects cannot be accurately accounted for with the dataset provided here as the location of the source of the emission is needed to establish the path through the specimen to the detectors. In future studies, X-ray yields should be recorded at each slice to enable these effects to be accounted for using methods such as those reported by Chen [13].

The electron beam used in the simulations did not include any undesirable aberrations such as defocus, spherical aberrations, chromatic aberrations, and astigmatism. These cannot be implemented in post-processing as they affect the interaction of the beam with the sample during propagation. Consequently, this tilt-series can be considered to provide a best-case limit of what would be achievable with a perfect lens system.

The tilt-series with a full 360° range could be considered to have a redundancy of 50%. For an ideal tomographic tilt-series this would be the case as diametrically opposed projections would be mirror images. However, as discussed above, STEM techniques do

not produce linear projections. The electron flux impinging on a certain atom depends on previous interactions with the specimen, this ‘top-bottom’ effect is particularly pronounced in channelling conditions [31]. Furthermore, after rotating the specimen, the focal plane of the electron beam in opposed projections is different, relative to the specimen. The comprehensive tilt-series reported here offers insights into these effects, and can be used to determine which of the available projections contain the most useful information, and which set of projections offers the minimum acquisition needed to perform certain analyses.

In providing a favourable dataset with a known ‘solution’, which nevertheless reflects the inherently challenging aspects of HAADF-STEM tomography, the tilt-series described here offers a valuable tool for the development of reconstruction and analysis methods and the optimization of acquisition procedures. All the simulated data, and the specimen model described in this paper are available from the authors on request.

The simulated data is provided in the form of MRC binary files [32]. A separate binary file is used for each characteristic X-ray map series, and for the HAADF series. The specimen model is provided as an XYZ file with the total number of atoms on the first line, followed by a blank line, then a line for each atom. These lines contain six tab separated values: the elemental symbol, the 3 Cartesian coordinates of the atom, the occupancy, and the mean square thermal displacement of the atom. The size of the total dataset is 2.2 GB.

## 8. Conclusion

The simulation of a tomographic tilt-series of HAADF-STEM images and EDS maps of a 22 nm integrated circuit device has been described. The model construction and multislice simulation methods have been discussed in detail. The simulated dataset alongside the well-defined specimen model provides a vital resource for the development and assessment of non-trivial three-dimensional reconstruction algorithms, and is available on request from the authors.

## Acknowledgments

The authors would like to thank Dr S Findlay for providing ionization scattering factors by private communication, and Remco Schoenmakers, Mark Williamson, Anna Carlsson, and Zhichao Zhong for useful discussions. This research is supported by the Dutch Technology Foundation STW (<http://www.stw.nl/>), which is part of the Netherlands Organization for Scientific Research (NWO), which is partly funded by the Ministry of Economic Affairs, Agriculture and Innovation under number 13314. This work is part of the research programme with project number SH-331-15, which is (partly) financed by the Netherlands Organisation for Scientific Research (NWO).

## References

- [1] R. Pantel, Coherent Bremsstrahlung effect observed during STEM analysis of dopant distribution in silicon devices using large area silicon drift EDX detectors and high brightness electron source, *Ultramicroscopy* 111 (11) (2011) 1607–1618.
- [2] D. Zanaga, T. Altantzis, L. Polavarapu, L.M. Liz-Marzn, B. Freitag, S. Bals, A. New, Method for quantitative xeds tomography of complex heterostructures, *Part. Part. Syst. Charact.* 33 (2016) 396–403.
- [3] P. Midgley, M. Weyland, 3D electron microscopy in the physical sciences: the development of Z-contrast and EFTEM tomography, *Ultramicroscopy* 96 (3–4) (2003) 413–431.
- [4] R. Aveyard, R. Ferrando, R.L. Johnston, J. Yuan, Modeling nanoscale

- inhomogeneities for quantitative HAADF STEM imaging, *Phys. Rev. Lett.* 113 (7) (2014) 075501.
- [5] T. Plamann, M.J. Hÿtch, Tests on the validity of the atomic column approximation for STEM probe propagation, *Ultramicroscopy* 78 (1999) 153–161.
- [6] W.V.D. Broek, A. Rosenauer, B. Goris, G.T. Martinez, S. Bals, S.V. Aert, D.V. Dyck, Correction of non-linear thickness effects in HAADF STEM electron tomography, *Ultramicroscopy* 116 (2012) 8–12.
- [7] J.M. Lebeau, S.D. Findlay, L.J. Allen, S. Stemmer, Quantitative atomic resolution scanning transmission electron microscopy, *Phys. Rev. Lett.* 100 (2008) 1–4.
- [8] C.J. Rossouw, V.M. Maslen, Implications of (e, 2e) scattering for inelastic electron diffraction in crystals II. application of the theory, *Philos. Mag. A* 49 (1984) 743–757.
- [9] S.T. Manson, Inelastic collisions of fast charged particles with atoms: ionization of the aluminum L-shell, *Phys. Rev. A* 6 (3) (1972) 1013.
- [10] D.K. Saldin, P. Rez, The theory of the excitation of atomic inner-shells in crystals by fast electrons, *Philos. Mag. B* 55 (1987) 481–489.
- [11] L.J. Allen, S.D. Findlay, M.P. Oxley, C.J. Rossouw, Lattice-resolution contrast from a focused coherent electron probe Part I, *Ultramicroscopy* 96 (1) (2003) 47–63.
- [12] C. Dwyer, Multislice theory of fast electron scattering incorporating atomic inner-shell ionization, *Ultramicroscopy* 104 (2) (2005) 141–151.
- [13] Z. Chen, A.J. D'Alfonso, M. Weyland, D.J. Taplin, L.J. Allen, S.D. Findlay, Ultramicroscopy energy dispersive x-ray analysis on an absolute scale in scanning transmission electron microscopy, *Ultramicroscopy* 157 (2015) 21–26.
- [14] E.J. Kirkland, *Advanced Computing in Electron Microscopy*, Second edition, Springer, 2010.
- [15] L.M. Voortman, L.J.V. Vliet, B. Rieger, When to use the projection assumption and the weak-phase object approximation in phase contrast cryo-EM, *Ultramicroscopy* 136 (2014) 61–66.
- [16] M.P. Oxley, L.J. Allen, Atomic scattering factors for K-shell and L-shell ionization by fast electrons, *Acta Crystallogr. Sect. A Found. Crystallogr.* 56 (5) (2000) 470–490.
- [17] S.D. Findlay, L.J. Allen, M.P. Oxley, **Additional Ionization Scattering Factors Made Available by Private Communication.**
- [18] W.T. Elam, B.D. Ravel, J.R. Sieber, A new atomic database for X-ray spectroscopic calculations, *Radiat. Phys. Chem.* 63 (2002) 121–128.
- [19] W. Xu, J. Dycus, X. Sang, J. LeBeau, A numerical model for multiple detector energy dispersive X-ray spectroscopy in the transmission electron microscope, *Ultramicroscopy* 164 (2016) 51–61.
- [20] O. Ugurlu, M. Strauss, G. Dutrow, J. Blackwood, B. Routh, C. Senowitz, P. Plachinda, R. Alvis, High-volume process monitoring of FEOL 22 nm FinFET structures using an automated STEM, *SPIE* 8681 (2013) 1–14.
- [21] L.-M. Peng, G. Ren, S.L. Dudarev, M.J. Whelan, Debye-waller factors and absorptive scattering factors of elemental crystals, *Acta Crystallogr. Sect. A Found. Crystallogr.* 52 (1996) 456–470.
- [22] Dien Li, X-ray absorption spectroscopy of silicon dioxide (SiO<sub>2</sub>) polymorphs: the structural characterization of opal, *Am. Mineral.* 79 (1994) 622–632.
- [23] R. Bassiri, F. Liou, M.R. Abernathy, A.C. Lin, N. Kim, A. Mehta, B. Shyam, R. L. Byer, E.K. Gustafson, M. Hart, I. MacLaren, I.W. Martin, R.K. Route, S. Rowan, J.F. Stebbins, M.M. Fejer, Order within disorder: the atomic structure of ion-beam sputtered amorphous tantalum (a-Ta<sub>2</sub>O<sub>5</sub>), *APL Mater.* 3 (2015) 036103.
- [24] C. Boothroyd, Quantification of high-resolution electron microscope images of amorphous carbon, *Ultramicroscopy* 83 (2000) 159–168.
- [25] C.J. Tavares, L. Rebouta, J.P. Rivière, T. Girardeau, P. Goudeau, E. Alves, N. P. Barradas, Atomic environment and interfacial structural order of TiAlN/Mo multilayers, *Surf. Coat. Technol.* 187 (2004) 393–398.
- [26] M. Scott, C. Chen, M. Mechlenburg, C. Zhu, R. Xu, C. Regan, J. Miao, P. Ercius, U. Dahmen, Electron tomography at 2.4 Å resolution, *Microsc. Microanal.* 18 (2012) 522–523.
- [27] J. Krehl, A. Lubk, Prospects of linear reconstruction in atomic resolution electron holographic tomography, *Ultramicroscopy* 150 (2015) 65–70.
- [28] W. van Aarle, W.J. Palenstijn, J. De Beenhouwer, T. Altantzis, S. Bals, K. J. Batenburg, J. Sijbers, The astra toolbox: a platform for advanced algorithm development in electron tomography, *Ultramicroscopy* (2015) 1–13.
- [29] W. Palenstijn, K. Batenburg, J. Sijbers, Performance improvements for iterative electron tomography reconstruction using graphics processing units (GPUs), *J. Struct. Biol.* 176 (2) (2011) 250–253.
- [30] C. Dwyer, C. Maunders, C.L. Zheng, M. Weyland, P.C. Tiemeijer, J. Etheridge, Sub-0.1 nm-resolution quantitative scanning transmission electron microscopy without adjustable parameters, *Appl. Phys. Lett.* 100 (2012) 0–4.
- [31] K. MacArthur, A. D'Alfonso, D. Ozkaya, L. Allen, P. Nellist, Optimal ADF STEM imaging parameters for tilt-robust image quantification, *Ultramicroscopy* 156 (2015) 1–8.
- [32] A. Cheng, R. Henderson, D. Mastrorarde, S.J. Ludtke, R.H.M. Schoenmakers, J. Short, R. Marabini, S. Dallakyan, D. Agard, M. Winn, MRC2014: extensions to the MRC format header for electron cryo-microscopy and tomography, *J. Struct. Biol.* 192 (2015) 146–150.